Mechanical properties of AlSi10Mg alloy fabricated by laser melting deposition and improvements via heat treatment

Article (Accepted Version)

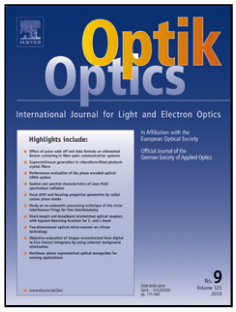

Title: Mechanical Properties of AlSi10Mg Alloy Fabricated by Laser Melting Deposition and Improvements via Heat Treatment

Authors: Fei Lv, Lida Shen, Huixin Liang, Deqiao Xie, Changjiang Wang, Zongjun Tian

PII: S0030-4026(18)31635-8
DOI: https://doi.org/10.1016/j.ijleo.2018.10.112
Reference: IJLEO 61737

To appear in:

Received date: 27-8-2018
Accepted date: 18-10-2018

Please cite this article as: Lv F, Shen L, Liang H, Xie D, Wang C, Tian Z, Mechanical Properties of AlSi10Mg Alloy Fabricated by Laser Melting Deposition and Improvements via Heat Treatment, *Optik* (2018), https://doi.org/10.1016/j.ijleo.2018.10.112

Mechanical Properties of AlSi10Mg Alloy Fabricated by Laser Melting Deposition and Improvements via Heat Treatment

Fei Lv[a,b], Lida Shen[a], Huixin Liang[a], Deqiao Xie[a], Changjiang Wang[c], Zongjun Tian[a,*]

[a]*College of Mechanical and Electrical Engineering, Nanjing University of Aeronautics and Astronautics, Nanjing, 210016*

[b]*Nanjing institute of advanced laser technology，Nanjing，Jiangsu 210038，China*

[c]*Department of Engineering and Design, University of Sussex, Sussex House, United Kingdom*

Zongjun Tian,

Phone: +86-18951793300

Fax: 025-84892520

Email: tianzj@nuaa.edu.cn

Abstract. Process optimization and heat treatment of AlSi10Mg aluminum alloy parts fabricated by laser melting deposition (LMD) based on coaxial powder feeding are conducted in this paper to improve manufacturing quality. The microstructures and mechanical properties of the LMD-built AlSi10Mg alloy parts are systematically investigated. Experimental results show the relative density of the block samples increase to 99.2% without larger pores and cracks after process optimization. The sample microstructures are found to display directional rapid solidification characteristics, with the Al-Si eutectic microstructure containing three microstructures being cellular, columnar dendrites and divergent dendrites. With solution and artificial aging heat treatments, Si atoms are rejected from the supersaturated Al matrix to form small Si granular particles. The heat treated samples display a uniform microstructure without heterogeneities and the microhardness remains stable at 118 HV. When the as-built sample is heat treated for solution time 2h, tensile strength increases from 292 MPa to 342 MPa due to the formation of strengthening phase Mg_2Si.

Keywords *Laser Melting Deposition (LMD); AlSi10Mg; Microstructure; Microhardness; Tensile property; Heat treatment*

1 Introduction

The alloy AlSi10Mg belongs to the hypoeutectic aluminum alloy of Al-Mg-Si series, and is in demand in aerospace and automotive industry applications due to a high level of specific strength, thermal conductivity and corrosion resistance [1-5]. Aluminum alloy components with large size and complex structure are commonly developed using the casting combined forging process, however, the disadvantages of this process include a long production cycle and high cost [6]. Laser melting deposition (LMD) is an additive manufacturing (AM) technique that can be used to produce metal parts [7]. Functional metal with fully dense parts is produced by depositing metal powders layer by layer using a laser beam as energy source and a closed-loop control system to maintain dimensional accuracy and material integrity [8-10]. Laser melting deposition compensates for the shortcomings of conventional manufacturing technology in the production of large size, complex shape and high performance structural parts which is why it has attracted considerable attention [11].

As an AM technique, LMD is a direct deposition process of energy transfer, powder transport and powder solidification. In recent years, many scholars have carried out research on materials of LMD including stainless steel [14], nickel base alloy [15], titanium alloy [16-17] and titanium alloy composite [18-19]. Laser melting deposition fabricated AlSi10Mg can however be a challenging material due to its high reflectivity, thermal conductivity and oxidation characteristics [20-21]. Process parameter optimization and post treatment are challenges in the study of LMD-AlSi10Mg which is why research on AlSi10Mg fabricated by laser melting deposition is rarely reported. Chen et al [22] fabricated thin plate-like 4045

aluminum alloy samples by LMD. They studied the microstructure evolution of the deposited samples before and after heat treatment and tested the microhardness of the samples. M.Javidani et al [23] researched the microhardness and microstructure of AlSi10Mg aluminum alloy with the LMD process. The relationship between the microstructure and mechanical properties of aluminum alloy fabricated by laser melting deposition, regardless of a post treatment or not, remains to be further studied. Li et al [24] revealed that the tensile strength and elongation of AM Al-Si-Mg alloys can be further tailored by controlling the morphology/coarsening of Si by adopting a specific heat treatment.

Typical heat treatment for Al-Si-Mg alloys is T6 heat treatment consisting of solution heat treatment, quenching and natural or artificial aging [25]. The solution heat treatment is conducted to dissolve soluble phases containing Mg or other trace elements, homogenize the composition and spheroidize the Si phase [26]. Quenching keeps the solutionized phase at a high temperature and suppresses precipitation, and a uniform distribution of precipitates is obtained after aging to strengthen the alloys [27]. Solution is carried out at an elevated temperature between 515°C and 530°C. Natural aging is undertaken at room temperature, while artificial aging is carried out at an elevated temperature between 150°C and 210°C.

In this paper, a brief summary of the AlSi10Mg LMD experimental procedure is provided, including details on process parameter optimization and heat treatment. Samples of AlSi10Mg are investigated and optimized based on microstructure analysis, hardness testing and tensile testing to improve mechanical properties. Following this, a systematic investigation is conducted on the influence of solution and artificial aging on microstructure and mechanical properties.

2. Experimental procedures

2.1 Materials and equipment

Gas atomized AlSi10Mg powder has an approximate spherical shape and size ranging from 50 µm to 130 µm, and a Gaussian distribution centered on 78 µm. This is shown in Fig. 1 and the chemical composition of AlSi10Mg alloy is presented in Table 1. The powder contains a large amount of small particles, which may negatively affect flowability due to the tendency of small particles to agglomerate. The small particles may however significantly increase the specific surface area of material, leading to high energy absorptivity of the laser beam [28].

Table1 Chemical compositions of AlSi10Mg powder (Wt%)

Si	Fe	Cu	Mg	Mn	Zn	Al
9.88	0.43	0.011	0.44	0.0086	0.01	bal

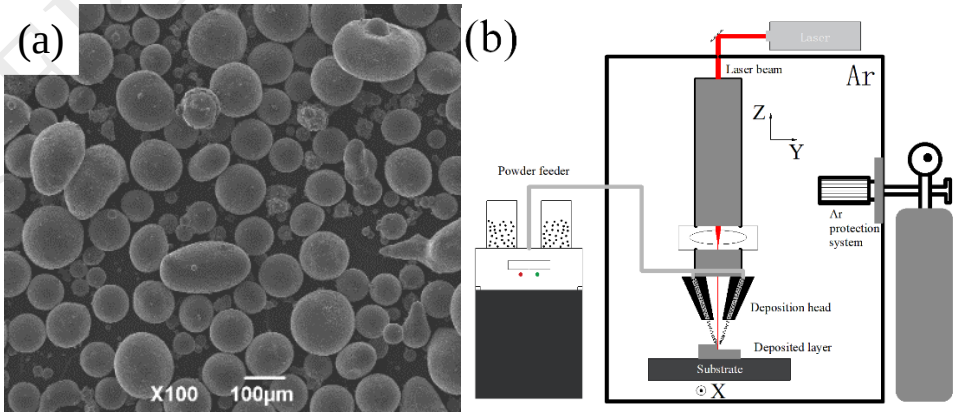

Fig. 1 Materials and equipment: (a) SEM micrograph of micro shape of AlSi10Mg powder. (b) Schematic diagram of Laser Melting Deposition equipment of LMD8060.

Samples were fabricated using a Raycham LDM8060 machine equipped with a rated output power of a 4 kW Laserline IPG fibre laser, as shown in Fig. 2(a). The laser beam diameter was approximately 3 mm. The AlSi10Mg powder was transported to the nozzle through the powder feeder, and the powder was melted by a laser beam. The building chamber was sealed

and purity argon gas was fed inside using an argon protection system, thereby decreasing the oxygen content below 50 ppm to avoid oxidation. Samples of a certain height are provided in Fig. 2(b).

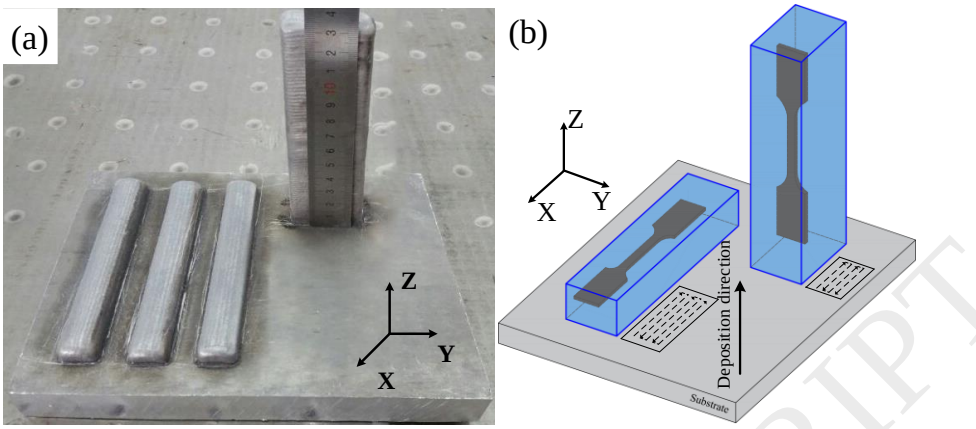

Fig. 2 (a) Laser melting deposited AlSi10Mg, (b) schematic diagram of the building sample

2.2 AlSi10Mg samples fabricated by LMD

The substrates used were ZL104 aluminum alloy. Before producing the samples, the substrates were ground and cleaned with ethanol. The powder was dried at a temperature of 373 K to reduce humidity and residual oxygen content.

The laser power used was 2000~3600 W at an interval of 400 W. The scanning speed was 360~840 mm/min, the interval was 120 mm/min and layer thickness was 0.5 mm. Several block samples with the dimension of 50×200×30 mm3 were fabricated under these guidelines to investigate the influence of processing parameters (laser power, scanning speed) on the densification rate, microstructure and tensile properties of as-built samples. The process parameters seen in Table 2 were used during the LMD process.

Table2 Process parameters

Laser power, P/W	Scanning speed, V/(mm/min)	Spot size, d/mm	Hatch distance, D/mm	Powder feed rate/(r/min)	Scanning strategy
2000~3600	360~840	3.5	1.5	1	'S'-shaped

2.3 Heat treatment

In accordance with the standard T6 heat treatment process, the as-built samples were solution treated at 525°Cunder varying times of 0.25h, 0.5h, 1h and 2h. This was followed by water quenching. After the solution treatment, the samples were immediately subjected to artificial aging at 180°Cfor 8h, then all samples were water quenched to room temperature [29].

2.4 Materials characterization

The samples were cut from the substrate with electrical discharge machining and the relative densities of these samples were measured by the Archimedes method [30]. All samples were successively ground using SiC papers from 200 down to 3000. After grinding, polishing was performed on the samples using polishing fabric and the polished surface was etched using Keller's reagent (HF-1 ml, HCl-1.5 ml, HNO3-2.5 ml and distilled water H2O-90 ml) for 15s.

The microstructures of the samples after etching were initially characterized by Leica CMS Gmbh optical microscopy. The microstructures were then examined using a Hitachi S-3400N II field emission scanning electron microscope (SEM) equipped with HORIBA EX-250 energy dispersive spectrometry (EDS). The chemical composition was analyzed by EDS. Image pro plus software was utilized for image analysis of the deposited samples to measure secondary dendrite arm spacing and size of Si particles. Phase analysis was carried out using a DMAX-

2500PC X-ray diffraction (XRD) spectrometer with Cu Kα radiation operated at 40 kV and beam current of 30 mA. A scanning speed of 2°/min was used for the scan range of 20-110°in steps of 0.02°. The microhardness of the samples was measured by HY HV-1000A using 10gf and a 10s indentation dwell time.

The tensile samples were produced in accordance with GB/T 16865-20131. Tensile tests were carried out using a WDW-100A universal material testing machine at a strain rate of 1×10-4s-1 and room temperature 300 K. Finally, the fracture morphology were sequentially characterized by a QUANTA 3D FEG field emission scanning electron microscope respectively.

3. Results and discussions

3.1 Characterization of samples

3.1.1 Relative density

To evaluate the combined effect of scanning speed V and laser power P during AlSi10Mg LMD process, laser line energy density L was defined by L = P/V. Fig. 3 illustrates the effect of laser power P and scanning speed V on the relative density of the as-built samples. With a low L applied during LMD (L=166.7J/mm), a large number of pores and un-melted particles are present on the microstructure of the as-built samples. This is predominantly caused by discontinuous scan tracks and the resultant interlayer pores, thereby yielding a relatively low densification level (93.9 %), as shown in Fig. 4(a). When the L increases to 200 J/mm and 266.7 J/mm, the cross-section of the as-built samples displays a fine microstructure with a very small amount of pores, implying a relatively high densification level (97.2 %) as displayed in Fig. 4(b) and Fig. 4(c). This high densification level is due to the increase of line energy density which more uniformly melts the powder. Surface tension and viscosity of the molten pool decreases sharply with the increase of temperature and fluidity, meaning the molten pool flows sufficiently. This causes the surface to be more smooth and flat with increased density. Interestingly, at an even higher L of 533.3 J/mm, the densification level of the as-built samples decreases significantly to 94.7%, as shown in Fig. 4(d). A large amount of pores are observed on the cross-sectional microstructures. Such a limited densification level is believed to be caused by poor interlayer bonding. The unstable surface of scan tracks caused by exorbitant line energy density results in the formation of interlayer pores, decreasing the densification level of the as-built samples.

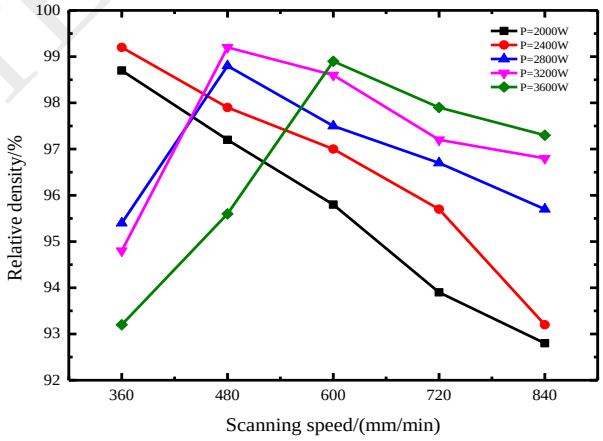

Fig. 3 Influence of process parameters on the relative density of LMD-built samples.

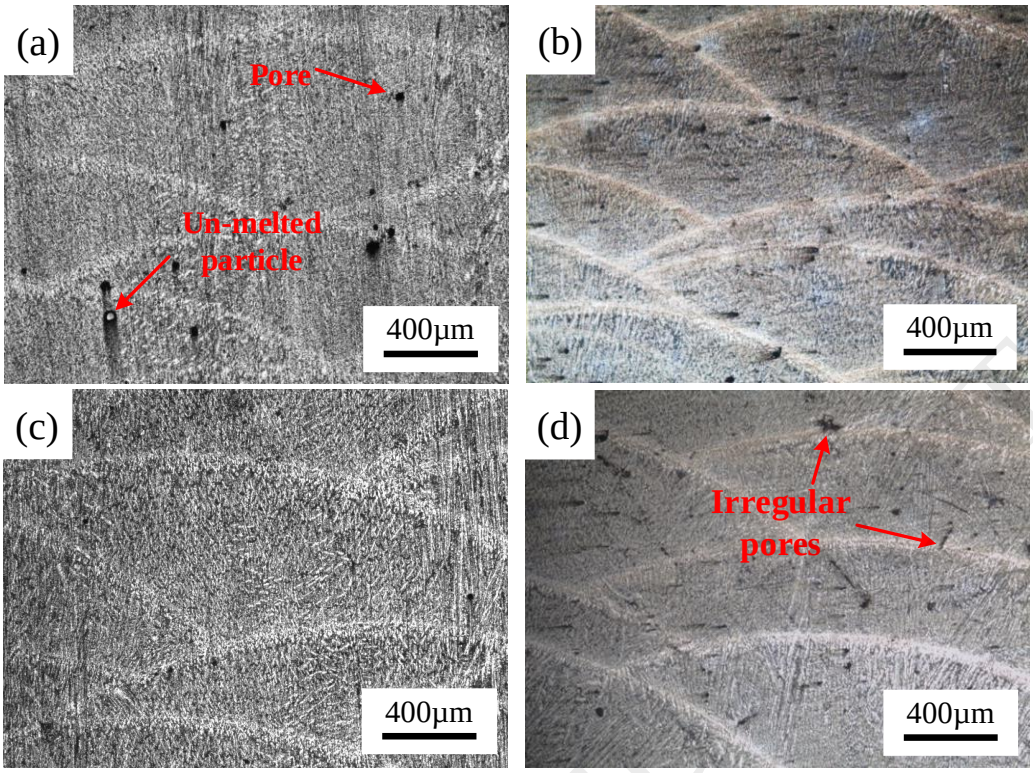

Fig. 4 OM microstructures of LMD-built samples under different parameters: (a) L=166.7J/mm; (b) L=200J/mm; (c) L=266.7J/mm; (d) L=533.3J/mm

3.1.2 Microhardness corresponding to microstructures

During LMD, the samples with L range of 200 J/mm~450 J/mm possess a relatively high densification level. The samples with L at 266.7 J/mm (P=3200 W, V=720 mm/min) are used to analyze the microstructure, as presented in Fig. 5.

Figure 5 displays typical OM micrographs in the longitudinal section (X-Z) of the as-built sample in three different locations of the deposit. These locations are (a), the bottom location of the sample (near the substrate); (b), the middle part location of the sample and (C), the top end of the sample. Although the dominant solidification structure is columnar dendrites, three different solidification structure features are established across the sample, depending on the distance of the deposited layers from the substrate. The principal solidification feature near the substrate is cellular, which is progressively substituted by a columnar dendrites structure when further away from the substrate. Subsequently, in the narrow zone at the topmost layer of the deposit, a divergent dendrites structure prevails.

The LMD process has the characteristics of fast cooling and high temperature gradient. It is a rapid solidification process. The heat of the deposited layers is released in three ways during process. First, it flows through the adjacent layers through conduction, then it flows to the substrate and finally, it is released into the surrounding atmosphere through radiation and convection. During the process, the heat flows mainly through the substrate and the adjacent deposited layers, and the effect through the atmosphere is weak. Depending on the location of the deposit in the LMD process, one or a combination of the three heat release processes dominate. The evolution of microstructures in different locations is affected by the cooling rate and the direction of the heat flow.

At the start of the deposition process, the substrate acts as a heat extractor for the first layers and the cooling rate is high. The microstructure is grown opposite to the heat flow direction and perpendicular to the solid/liquid interface forming the cellular microstructure, as shown in Fig. 5(a). As the number of deposited layers increases, the influence of the substrate became negligible. In progressively moving further away from the substrate, the role of the adjacent solidified layer in heat release is gradually enhanced. The heat accumulation phenomenon gradually becomes more significant and the cooling rate is reduced. A smooth

and gradual transition of microstructure from cellular to columnar dendrites is roughly established, as shown in Fig. 5(b). Eventually, at the top end, the heat accumulation phenomenon is the most significant, the influence of substrate is weak and the role of the surrounding atmosphere in heat release is enhanced. Instead of growing in a unified solidification direction, the dendrites, are observed to grow in multiple directions and the microstructure transited to the divergent dendrites. Moreover, the size of the Si eutectic particles in this location is much greater than those in the columnar dendrites region, as illustrated in Fig. 5(c).

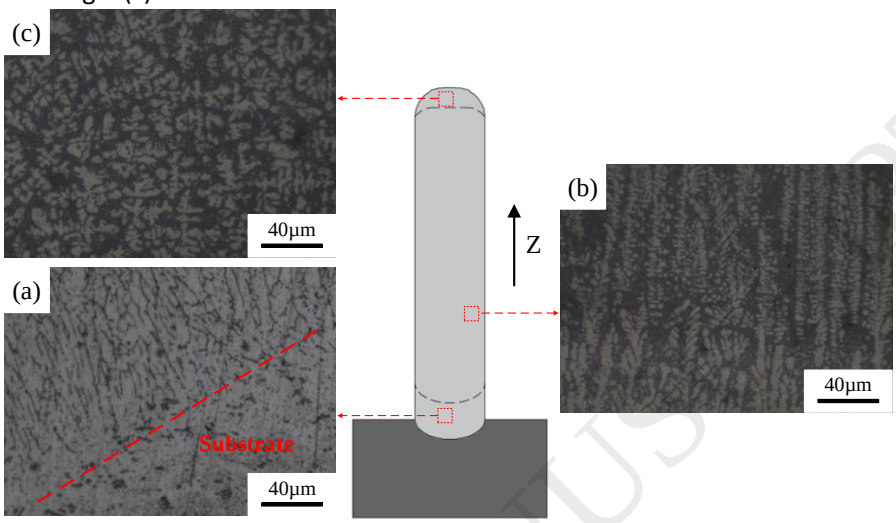

Fig. 5 OM microstructures of LMD-built samples in different locations: (a) Bottom location near the substrate; (b) Middle part location; (c) Top end.

Microhardness tests were conducted to determine the microhardness along the deposition direction. Fig. 6 presents the variations of microhardness (HV) across the sample from the bottom to the top end. As shown in Fig. 6, the deposit is classified into three major locations based on the presented hardness profile. The highest hardness value, with an average of ~122 HV, was obtained in the location near the substrate which is characterized by a fine cellular structure. In moving further away from the substrate and transitioning to the region with a dendrites structure, the microhardness was reduced to an average value of ~111 HV. The microhardness value remained relatively stable across the columnar dendrites region. Further away from the substrate, entering the region with a divergent dendrites structure, the average microhardness value was ~100 HV.

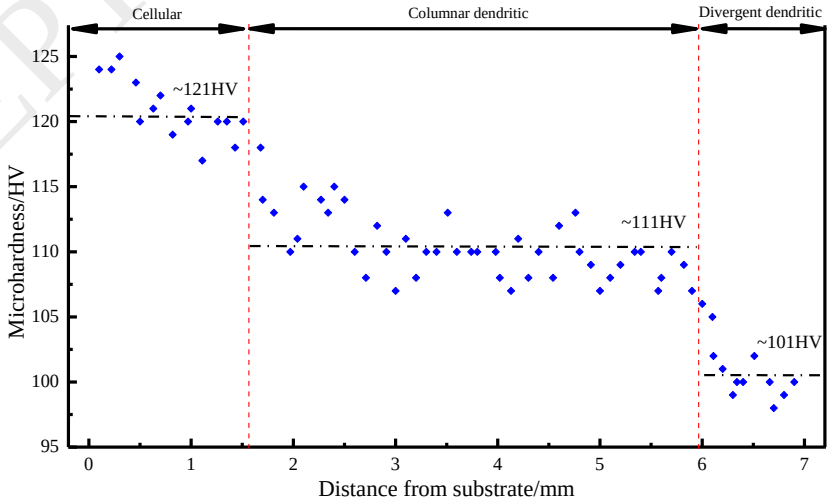

Fig. 6 Variation of microhardness all over of the sample from bottom location to top end

3.1.3 Analysis of solution strengthening

During solidification of AlSi10Mg, the Si phase was initially solidified into the solid phase and expelled into the liquid phase at the solid/liquid interface front. As solubility of Si in Al was extended due to the rapid cooling rate, the Si were supersaturated in Al matrix, as shown in Fig. 7(d). The Si content in Al matrix is about 7.6 wt.% which is more than the maximum saturation of Si in Al matrix (1.65%)[31]. Solid solution strengthening, caused by the supersaturated solid solution of Si in the Al matrix for LMD AlSi10Mg, improved the mechanical properties of LMD-built samples.

The relationship between the secondary dendrite arm spacing (SDAS) l and cooling rate R_c can be expressed by [32-33]:

$$l = B(R_c)^{-n} \quad (1)$$

where B and n are proportionality constant, B=47 and n=0.33. It is clear that SDAS increases with the decreasing cooling rate R_c (with decreasing scanning speed). Figure 7 shows the SEM micrographs of microstructures viewed along the cross section of AlSi10Mg samples produced by LMD (P=3200W, V=480 mm/min, 600 mm/min and 720 mm/min). The SDAS are 3.24 μm, 2.99 μm and 2.65 μm. According to Eq. (1), the cooling rates are 3310 K/s, 4222 K/s and 6087 K/s respectively. The Si solid solubility in Al matrix was enhanced by increasing the scanning speed. The EDS analyses of the label '1' and '2' in Fig. 7(a) and (c) are shown in Fig. 7(d) and (e) respectively. As illustrated in Fig. 7(d)-(f), at a laser power of P=3200 W, the Si content increased from 6.21 wt.% to 7.62 wt.% with the scanning speed increasing from 480 mm/min to 720 mm/min. The Si content increased in the Al matrix, and the effect of solid solution strengthening is enhanced. However, with the increase of scanning speed, the defects in microstructure increase and influence the mechanical properties.

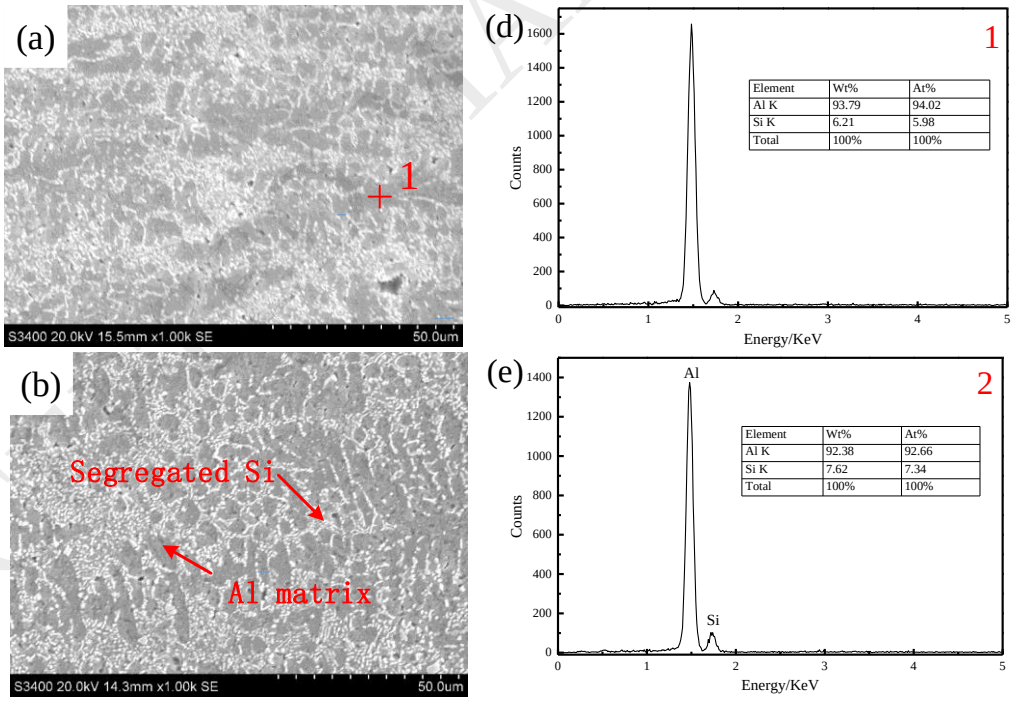

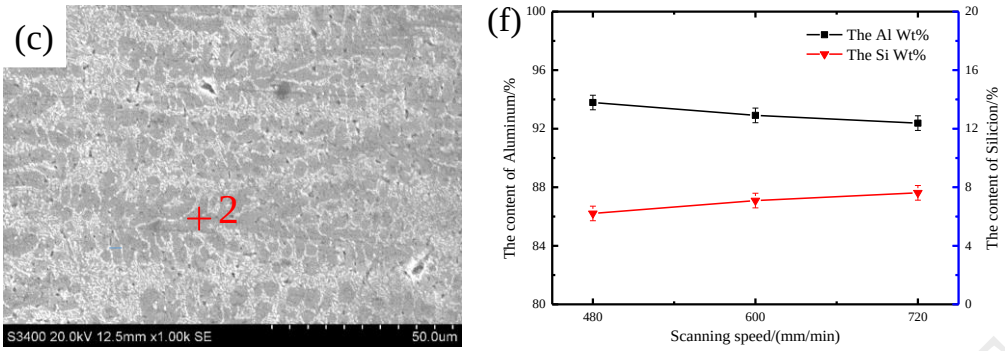

Fig. 7 SEM microstructure of LMD-built samples under different scanning speed: (a) V=480mm/min; (b) V=600mm/min; (c) V=720mm/min; (d), (e) The EDS analyses of the label '1' and '2' in (a) and (c) respectively; (f) the influence of scanning speed on the concentration of element.

3.1.4 Tensile property of as-built samples

The tensile samples were produced by LMD using a constant laser power of P=3200 W and various scanning speed of V=480, 600, 720 and 840 mm/min. Figure 8(b) shows that the maximum ultimate tensile strength and tensile strain of LMD-built AlSi10Mg samples is influenced by scanning speed. With the increase of scanning speed, the tensile strength of the sample first increases and then decreases. When the scanning speed is 720 mm/min, the tensile strength is 292 MPa. Figure 10(a) shows these stress-strain curves.

As shown in Fig. 3 and Fig. 8(b), with an increase of scanning speed, densification level is reduced, but tensile strength is improved. This is because the increase of scanning speed can speed up the cooling rate and enhance the solid solution strengthening effect under the premise that the energy absorbed by materials is sufficient. This process is illustrated in Fig. 7(d) and (e). The increase of scanning speed is beneficial to improve the tensile properties of the samples. With further intensification of scanning speed, the effect of internal defects dominates and the tensile strength is lowered.

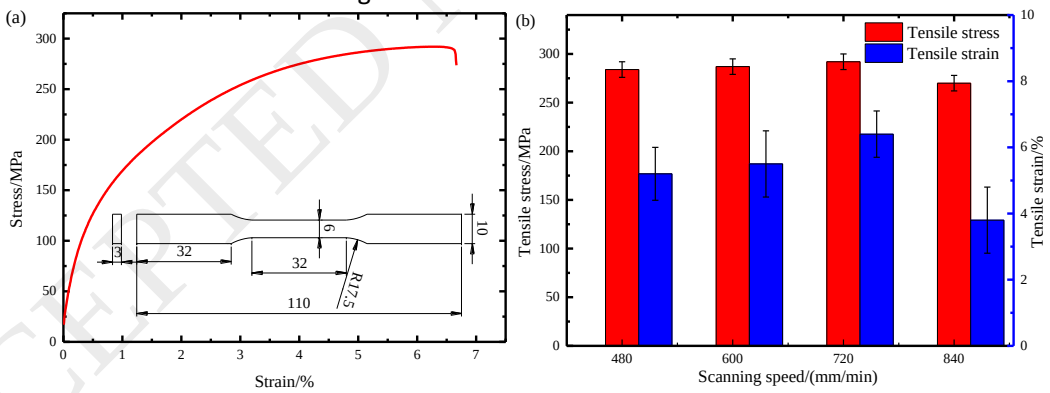

Fig. 8 The relationship curve of the tensile property: (a) Tensile stress test curve at V=720mm/min; (b) Influence of the scanning speed on the tensile strength and ductility

The analysis of the tensile properties presented in Fig. 9 allows for the rationalization of fracture morphologies for the different samples. From Fig. 9(a) and (b), it can be seen that a number of dimples are visible on the fracture surface of AlSi10Mg samples produced by LMD using laser power of 3200 W and scanning speed of 720 mm/min. The fracture surfaces are relatively smooth, macroscopic plastic deformation is slight, and there is a significant cleavage morphology exhibiting a quasi-cleavage type of fracture. This result implies that an AlSi10Mg sample with a relatively high tensile strength can be obtained by LMD using laser power of 3200 W and scanning speed of 720 mm/min. As the scanning speed increases to 840 mm/min, the fracture surfaces become more irregular and consist of a large number of pores, interlayer interface and un-melted particles, as shown in Fig. 9(c) and (d). These pores and un-melted particles create complex fracture surfaces, lowering the tensile strength of LMD built samples.

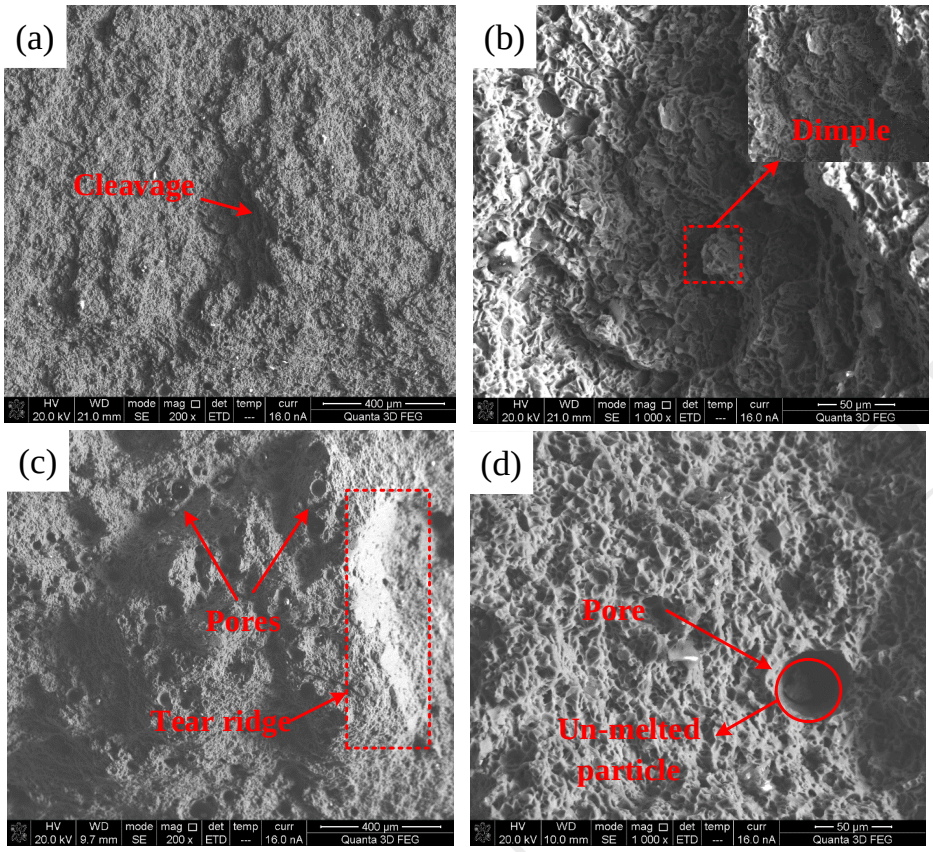

Fig. 9 SEM fracture micrographs of tensile samples: (a), (b) P=3200W， V=720mm/min；(c), (d) P=3200W， V=840mm/min.

3.2 Heat treatment of samples

3.2.1 Microstructure characterization

The new samples were prepared according to the optimized parameters and then heat treated. The heat treatment process is described in the previous section. The two main functions of heat treatment for as-built samples are to eliminate anisotropy and to induce strengthening phase precipitation by artificial aging treatment.

Fig. 10 depicts the SEM micrographs of the microstructure of heat treated LMD AlSi10Mg samples. The effect of solution and artificial aging heat treatment on the microstructure is also shown. After heat treatment, the eutectic silicon undergoes spheroidizing. A fine granular phase is then dispersed uniformly in the α-Al matrix. The heat treatment sample displays a uniform microstructure without heterogeneities resulting from the temperature gradient. In increasing the solution time from 0.25h to 2h, the fragmentizing and spheroidizing of silicon becomes more complete. To investigate the change in size of the Si particles upon heat treatment, detailed image analysis was conducted on SEM micrographs obtained from different heat treatment conditions. When the LMD-built AlSi10Mg is solution heat treated for 0.25h, most of the Si particles are less than 1 μm. With the increase of solution time from to 2h, some of the Si particles are coarsened, with a diameter increase from 2 to 4 μm.

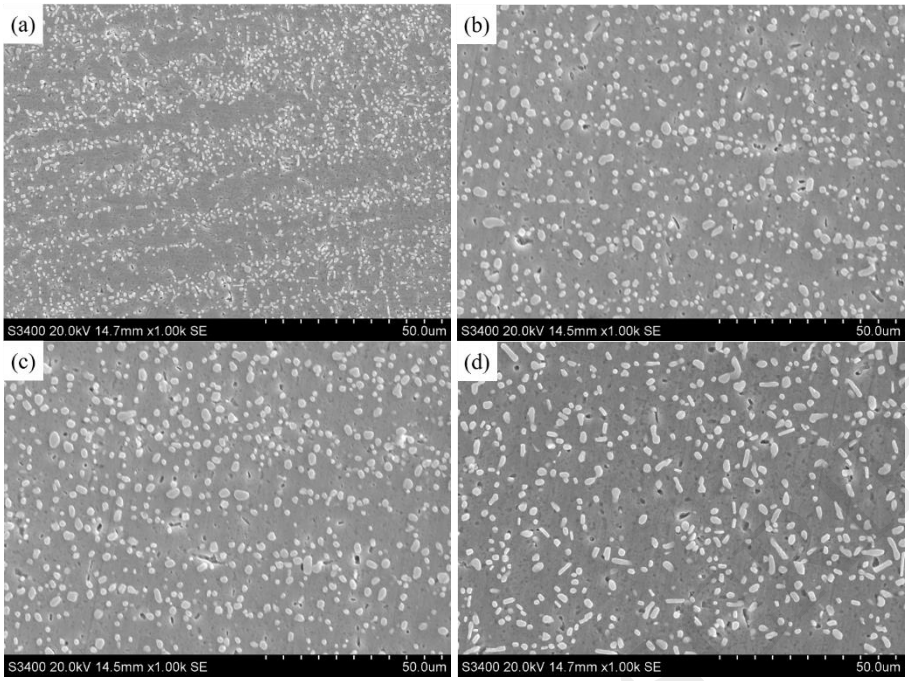

Fig. 10 SEM micrographs of the eutectic microstructures of the LMD-built AlSi10Mg under different solution time: (a) 0.25h; (b) 0.5h; (f) 1h; (g) 2h.

The uniform distribution of Si particles in the microstructure of the heat treatment samples is likely due to the spheroidizing of Si phase [34]. According to Ostwald ripening theories, the spheroidizing of Si phase is a process of fusing, fragmentizing, ripening and growing at bifurcation or constricted regions. The process is activated through the diffusion of Si atoms at the Al/Si interface. It is possible to schematically describe the microstructure evolution of the LMD-built AlSi10Mg samples during heat treatment which is shown in Fig. 11. As discussed, the as-built LMD sample displays a microstructure consisting of supersaturated Al matrix decorated with dendritic Si phase (red arrows in Fig. 11), denoted by phase A. Following solution heat treatment and artificial aging, Si is rejected from the supersaturated Al to form small Si particles denoted by phase B. At this stage the dendritic boundaries become blurred. With an increase in the solution time, the Si particles generally precipitate along the Al-Si boundaries and fragmentize and spheroidize significantly. Finally, the granular Si particles are evenly distributed on the surface of the Al matrix, which is denoted by phase C.

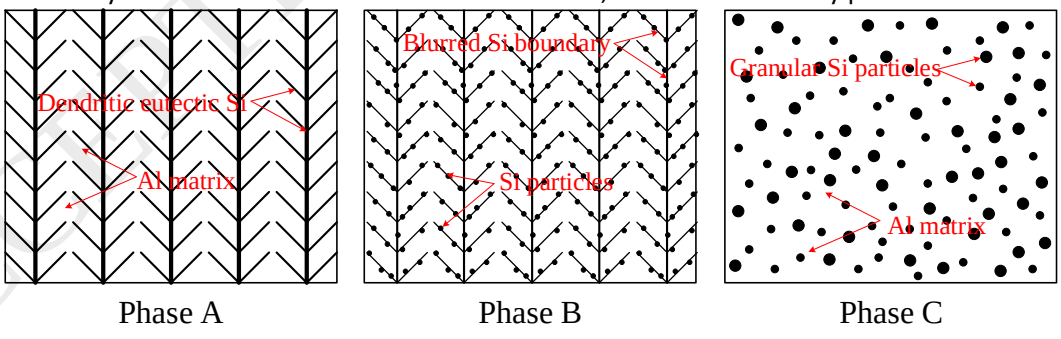

Fig. 11 Schematic of the microstructure evolution of the LMD-produced AlSi10Mg samples during the solution and artificial aging heat treatment.

3.2.2 XRD analysis

The XRD results of the as-built and heat treated LMD samples are presented in Fig. 12. The Mg_2Si XRD peak intensity of the as-built LMD sample is lower than that of the heat treated samples. This result is mainly attributed to Si precipitating out from the Al matrix after heat treatment and then separated Si reacting with Mg to form the Mg_2Si phase [35]. However, the Mg_2Si peaks with an increase of solution time remain unchanged. This is likely due to the low content of Mg (0.4–0.5 wt %) in AlSi10Mg alloy. Although the samples precipitate more Si,

there is no residual Mg left to form further Mg_2Si phase [36], indicating that Mg is a limited reactant for generating the Mg_2Si phase. This Mg_2Si phase is considered a strengthening mechanism in Al-Si-Mg cast alloys.

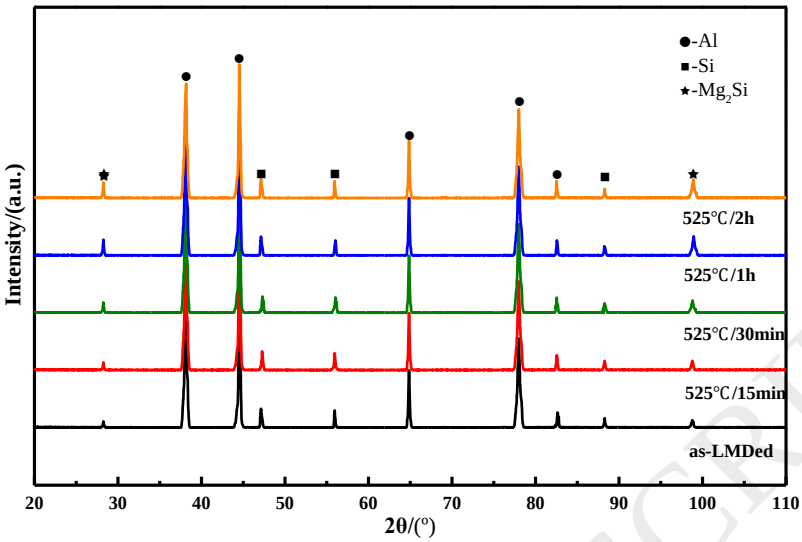

Fig. 12 XRD patterns of the LMD AlSi10Mg samples fabricated under different solution time.

3.2.3. Mechanical properties after heat treatment

To evaluate the influence of heat treatment on the hardness and tensile strength of the as-built LMD AlSi10Mg samples, microhardness and tensile strength tests were introduced. The solution and artificial aging heat treatment has a great influence on the mechanical properties. In general, the microhardness values of the heat treated samples (118±5 HV) are lower than the those of the as-built ones, but the hardness from bottom location to top end remain equal. The hardness of as-built samples changed greatly depending on location. This result can be attributed to the coalescence and diffusion of Si phase as well as Ostwald ripening. The uniform distribution of the Si particles caused by this phenomenon, bring about continuity in the mechanical properties.

The variations of tensile strength with solution time is given in Fig. 13. The sample with solution time of 2h exhibits the highest tensile strength of 342 MPa. When the sample is solution heat treated for 15min, there is a slight increase in tensile strength (302 MPa). With further increase of the solution time to 30min, the tensile strength is raised to 315 MPa and with the solution time of 1h, the sample exhibits the tensile strength of 340 MPa.

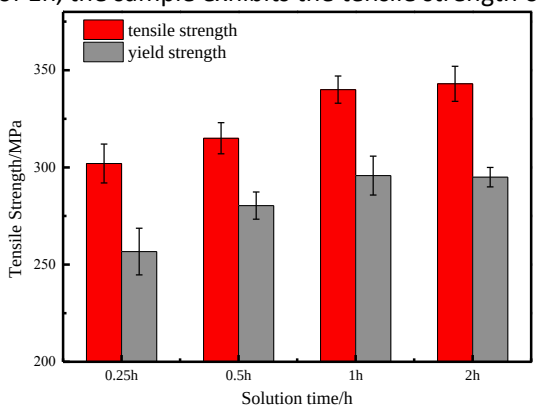

Fig. 13 Tensile strength of the heat treated LMD samples

The high strength of the heat treated LMD AlSi10Mg samples can be attributed to precipitation strengthening of strengthening phase Mg_2Si. It is the reaction of Mg with Si that causes the precipitation process in which a fine distribution of precipitates interact with dislocations and yield the reaction of Mg with Si. This provokes the precipitation process in which a fine distribution of precipitates interact with dislocations and provide the desired

strengthening. The precipitation occurs in several stages. First, small clusters and Guinier-Preston zone of Mg and Si atoms are formed. Then, Mg_2Si precipitates nucleate in the form of metastable and coherent phases, which gradually change into metastable and semi-formed phases. Next, Mg_2Si precipitates nucleate in the form of metastable and coherent phases which slowly transform into metastable and semicoherent phases, providing the maximal strengthening effect.

Thermally stable Mg_2Si particles uniformly distribute in the matrix of the AlSi10Mg. The particles contribute more effectively to dislocation hardening by pinning and thus further enhancing the formation of dislocation cell networks within the deformed grains. This phenomenon can block the motion of dislocations, resulting in an elevated work-hardening rate along with a resultant high ultimate tensile strength. However, when solution time is increased from 1h to 2h, the tensile strength changes little as there is not enough Mg reacting with Si to generate Mg_2Si. This phenomenon also validates the effect of the strengthening phase Mg_2Si.

4. Conclusions

In this study, process optimization was conducted on the LMD-built AlSi10Mg samples using various processing parameters. The effects of solution and artificial aging heat treatments on the phase, microstructure and mechanical properties of the LMD-built AlSi10Mg samples were systematically studied. The main results and findings are as follows.

(1) During LMD, the L range of 200 J/mm~450 J/mm was the best scope of technique parameters to produce AlSi10Mg samples with a densification rate up to 99.2% and no large size defects in the microstructures.

(2) From the substrate to the top end, there are three solidification structures. These are cellular near the substrate, columnar dendrites at the middle part location and divergent dendrites at the top end. Microhardness decreased gradually from the bottom location to the top end with the transition of microstructures.

(3) Upon solution and artificial aging heat treatment, Si atoms precipitated from the supersaturated Al matrix to form small granular Si particles. A fine granular phase was dispersed uniformly in the α-Al matrix through the spheroidizing of Si phase. In increasing the solution time, the size of the Si particles increased.

(4) Following heat treatment, the microhardness from the bottom location to the top end remained equal at 118 HV, which is attributed to the uniform distribution of Si particles. The tensile strength for the as-built samples increased from 292 MPa to 342 MPa for the samples heat treated for solution time 2h, due to precipitation strengthening of strengthening phase Mg_2Si.

Acknowledgments

The work was financially supported by the Advanced Research Project of Army Equipment Development(301020803), the Key Research and Development Program of Jiangsu (BE2015161), the Young Scientists Fund of the National Natural Science Foundation of China(51605473), the Jiangsu Provincial Research Foundation for Basic Research, China (BK20161476), the Science and Technology Planning Project of Jiangsu Province of China (BE2015029) and the Science and Technology Support Program of Jiangsu (BE2014009-1, BE2014009-2, BE2016010-3).

References

[1] Cole G S, Sherman A M. Light weight materials for automotive applications ☆. Materials Characterization, 1995, 35(1):3-9.

[2] Vrancken B, Thijs L, Kruth J P, et al. Heat treatment of Ti6Al4V produced by Selective Laser Melting: Microstructure and mechanical properties. Journal of Alloys & Compounds, 2012, 541(541):177-185.

[3] R. Mahshid, H.N. Hansen, K.L. Højbjerre. Strength analysis and modeling of cellular lattice structures manufactured using selective laser melting for tooling applications. Materials & Design, 2016, 104:276-283.

[4] PIKETT A K, PYTTEL T, PAYEN F. Failure prediction for advanced crashworthiness of transportation vehicles. International Journal of Impact Engineering, 2004,30：853-872.

[5] B. Li, H.W.Wang, J.C.Jie, et al. Effects of yttrium and heat treatment on the microstructure and tensile

properties of Al-7.5Si-0.5Mg alloy, Materials & Design. 2011,32: 1617–1622.
[6] Yadroitsev I, Shishkovsky I, Bertrand P, et al. Manufacturing of fine-structured 3D porous filter elements by selective laser melting. Applied Surface Science, 2009, 255(10):5523-5527.
[7] Wang H M, Zhang L Y, Li A, et al. Progress on laser melting deposition processing and manufacturing of advanced aeronautical metallic structural materials and coatings. Heat Treatment of Metals, 2008, 33(1):82-85.
[8] Lu B H, Li D C Development of the Additive Manufacturing(3D printing)Technology. Machine Building & Automation, 2013.
[9] Zuo T C. Advanced manufacturing in twenty-first century. Beijing: Science Press, 2007.
[10] Zhang D Y. Review of laser direct manufacturing for metallic parts. China Mechanical Engineering, 2006(z1):434-438.
[11] Bi G, Sun C N, Nai M L, et al. Micro-structure and Mechanical Properties of Nano-TiC Reinforced Inconel 625 Deposited using LAAM ☆. Physics Procedia, 2013, 41(30):828-834.
[12] Wang H M, Zhang S Q, Wang X M, et al. Progress and Challenges of Laser Direct Manufacturing of Large Titanium Structural Components (Invited Paper). Chinese Journal of Lasers, 2009, 36(12):3204-3209.
[13] Chen D N, Liu T T, Liao W H, et al. Temperature Field During Selective Laser Melting of Metal Powder Under Different Scanning Strategies. Chinese Journal of Lasers, 2016, 43(4): 0403003.
[14] Wang C J, Liang J , Chen S Y, et al. Study on Microstructures and Properties of Direct Laser Deposited 15Cr21Ni7-xMo Stainless Steels. Applied Laser, 2017(1):11-16.
[15] Li J B, Shang S , Sun Y Z, et al. Parameter Nondimensionalization in Laser Direct Metal Deposition Formation of Inconel 625 and Its Influence on Single Track Geometric Morphology. Chinese Journal of Lasers, 2017, 44(3): 0302010.
[16] Xi M Z, Gao S Y. Heat-Treated Microstructures and Mechanical Properties of TA15 Titanium Alloy Fabricated by Laser Rapid Forming. Chinese Journal of Lasers, 2012, 39(1):0103007.
[17] Huang B Y, Li H X, Zhang Y B, et al. Formability of TC11 Titanium Alloy Fabricated by Direct Laser Deposition. Rare Metal Materials & Engineering, 2013, 42:178-182.
[18]Sun J C, Zhang Y Z, Huang C, et al. Microstructure and High Temperature Tensile Properties of Laser Direct Deposited Ti60 Alloy and TiC_P/Ti60 Composites. Chinese Journal of Lasers, 2011, 38(3):0303004.
[19] Sun J C, Zhang Y Z, Gong X Y, et al. High-Temperature Tensile Rupture Life and Fracture Procedure of Laser Direct Deposited Ti60 Alloy and TiC_p/Ti60 Composites. Chinese Journal of Lasers, 2012, 39(1):0103002.
[20] Zhang N W, Tang Y M. A new manual of practical metal materials. Shandong: Shandong science and technology press, 2010.
[21] Li N K, Ling G, Nie B, et al. Aluminum alloy material and heat treatment technology. Beijing: Metallurgical Industry Press, 2014.
[22] Chen Y C, Zhang S Q, Tian X J, et al. Microstructure and Microhardness of 4045 Aluminum Alloy Fabricated by Laser Melting Deposition. Chinese Journal of Lasers, 2015, 42(3): 0303008.
[23] Javidani M, Arreguin-Zavala J, Danovitch J, et al. Additive Manufacturing of AlSi10Mg Alloy Using Direct Energy Deposition: Microstructure and Hardness Characterization. Journal of Thermal Spray Technology, 2016:1-11.
[24] Li X P, Wang X J, Saunders M, et al. A selective laser melting and solution heat treatment refined Al–12Si alloy with a controllable ultrafine eutectic microstructure and 25% tensile ductility. Acta Materialia, 2015, 95:74-82.
[25] Sjölander E, Seifeddine S. The heat treatment of Al–Si–Cu–Mg casting alloys. Journal of Materials Processing Technology, 2010, 210(10):1249-1259.
[26] Moustafa M A, Samuel F H, Doty H W. Effect of solution heat treatment and additives on the microstructure of Al-Si (A413.1) automotive alloys. Journal of Materials Science, 2003, 38(22):4507-4522.
[27] Zhou L, Mehta A, Schulz E et al. Microstructure, precipitates and hardness of selectively laser melted AlSi10Mg alloy before and after heat treatment. Materials Characterization, 2018: 0-13.
[28] Zhu H H, Fuh J Y H, Lu L. The influence of powder apparent density on the density in direct laser-sintered metallic parts. International Journal of Machine Tools & Manufacture, 2007, 47(2):294-298.
[29] Li Y, Gu D. Parametric analysis of thermal behavior during selective laser melting additive manufacturing of aluminum alloy powder. Materials & Design, 2014, 63(2):856-867.
[30] Spierings A B, Schneider M, Eggenberger R. Comparison of density measurement techniques for additive manufactured metallic parts. Rapid Prototyping Journal, 2011, 17(5):380-386.
[31] Basariya M R, Srivastava V C, Mukhopadhyay N K. Microstructural characteristics and mechanical properties of carbon nanotube reinforced aluminum alloy composites produced by ball milling. Materials & Design, 2014, 64(9):542-549.
[32] Dinda G P, Dasgupta A K, Mazumder J. Evolution of microstructure in laser deposited Al–11.28%Si alloy. Surface & Coatings Technology, 2012, 206(8–9):2152-2160.
[33] Jarfors A E W. Solidification behaviour of Al–7% Si–0.3% Mg during rotary spray forming. Journal of Materials Science, 1998, 33(15):3907-3918.
[34] Li W, Li S, Liu J, et al. Effect of heat treatment on AlSi10Mg alloy fabricated by selective laser melting: Microstructure evolution, mechanical properties and fracture mechanism. Materials Science & Engineering A, 2016, 663:116-125.

[35] Xie X, Shen J, Cheng L, et al. Effects of nano-particles strengthening activating flux on the microstructures and mechanical properties of TIG welded AZ31 magnesium alloy joints. Materials & Design, 2015, 81:31-38.
[36] Izcara X L, Blank A G, Pyczak F, et al. Characterization and modeling of the influence of artificial aging on the microstructural evolution of age-hardenable AlSi 10 Mg(Cu) aluminum alloys. Materials Science & Engineering A, 2014, 610(29):46-53.